

FULL PAPER

A multi-resolution weighted compact nonlinear scheme for hyperbolic conservation laws

Huaibao Zhang,^{a,c} Guangxue Wang,^{a,d,*} and Fan Zhang^b

^aSchool of Physics, Sun Yat-sen University, Guangzhou 510006, China

^bCentre for mathematical Plasma-Astrophysics, Department of Mathematics, KU Leuven, Celestijnenlaan 200B, 3001 Leuven, Belgium

^cState Key Laboratory of Aerodynamics, China Aerodynamics Research and Development Center, Mianyang 621000, China

^dCollege of Aerospace Science and Engineering, National University of Defense Technology, Changsha 410073, China

ARTICLE HISTORY

Compiled February 7, 2020

ABSTRACT

A typical weighted compact nonlinear scheme (WCNS) uses a convex combination of several low-order polynomials approximated over selected candidate stencils of same width, achieving non-oscillatory interpolation near discontinuities and high order accuracy for smooth solutions. In this paper, we present a new multi-resolution fifth-order WCNS by making use of the information of polynomials on three nested central spatial sub-stencils having first-, third- and fifth-order accuracy, respectively. The new scheme is capable of obtaining high-order spatial interpolation in smooth regions, and it is characterized by the feature of gradually degrading from fifth-order down to first-order accuracy as large stencils deemed to be crossing strong discontinuities. The advantages of the present scheme include the superior resolution for high-wavenumber fluctuations and the flexibility of implementing different numerical flux functions.

KEYWORDS

weighted compact nonlinear schemes; multi-resolution; nested central stencil; hyperbolic conservation laws; compressible flows

1. Introduction

Second-order accurate schemes are no doubt the dominating tools for most industrial computational fluid dynamics (CFD) applications Wang et al. (2013). High-order schemes (third order accurate or higher), however, have received considerable attention in the CFD research community over the past decades, not only because they can effectively reduce numerically-induced dissipation and dispersion errors compared with low-order schemes Lele (1992), but yield high-resolution properties which are essential for the simulation of complex flow problems Johnsen et al. (2010); Ritos et al. (2018); Dong et al. (2019).

Besides the well-known WENO schemes Liu et al. (1994); Jiang and Shu (1996); Borges et al. (2008); Sun et al. (2016), another popular family of high-order numerical methods is the weighted compact nonlinear schemes (WCNSs) proposed by Deng and Zhang (2000). Being an extension of the compact nonlinear scheme (CNS) Deng and Maekawa (1997), a WCNS combines the advantages of both the nonlinear weighting technique in WENO schemes Liu et al. (1994), and the spectral-like resolution of compact schemes proposed by Lele (1992), therefore yields its great success by achieving robust shock-capturing properties and excellent resolution for

* Corresponding author. Email: wanggx7@mail.sysu.edu.cn

high-frequency waves.

Application of the classical WCNS consists of three steps Deng and Zhang (2000): (1) node-to-midpoint weighted nonlinear interpolation of flow variables – primitive variables for instance, (2) evaluation of flux terms at midpoints, and (3) midpoint-to-node centered flux differencing. As aforementioned, the strategy of nonlinear weighting, originating from WENO schemes Liu et al. (1994), is commonly used, in the first step, thereby the classical WCNS using the nonlinear weight of Jiang and Shu (1996) is often referred to as WCNS-JS. Moreover, among the three steps listed above, the node-to-midpoint interpolation procedure is essential for the shock capturing capability and multi-scale wave resolution of WCNSs Yan et al. (2016); Zheng et al. (2019). It has therefore been attracting much attention.

Recently, focusing on improving the performance of the nonlinear interpolation, a stencil selection method was incorporated in WCNS, resulting in a new compact nonlinear scheme Zhang et al. (2019), exhibiting reduced numerical dissipation and dispersion. In particular, the flux differencing used in the third step is performed using an explicit scheme, as in the WCNS-E-5 of Deng (2002). As suggested by Deng et al. (2005), for a WCNS, the nonlinear interpolation in step (1) dominates the resolution property; and explicit centered differencing, which does not need tridiagonal inversion for derivative calculations, is favored due to simplicity of implementation and superior computational efficiency. Further work of Nonomura and Fujii (2009) demonstrated that the type of flux differencing employed does not significantly change resolution, even for higher-order WCNSs. Therefore, in the present work, only the nonlinear interpolation is discussed, and an explicit differencing formula is applied without further investigating the details.

Despite that much of the attention was given to improved nonlinear weighting itself, some efforts were focused on strong robustness of numerical schemes especially for compressible flow problems involving severe discontinuities. One typical instance is the so-called multi-dimensional optimal order detection (MOOD) strategy Clain et al. (2011), which is promising to obtain oscillation-free results, since strongly stable first-order interpolation is allowed in case high-order interpolations fail to do so. Recently, Zhu and Shu (2018) proposed a multi-resolution strategy that instead of using sub-stencils of equal-size, the high-order scheme is developed using polynomials on a set of nested central spatial sub-stencils. These polynomials have first-, third-, fifth-, and even higher order of accuracy if any, respectively. This strategy allows the variable interpolation gradually degrading from high-order down to first-order accuracy as large stencils deemed to be crossing strong discontinuities. Thus, strong stability can be achieved in such cases. Zhang et al. (2018) also designed a ENO-type framework to exploit the potential of using gradually degraded stencils. In this work, we develop a new WCNS by incorporating this specific multi-resolution strategy of Zhu and Shu (2018), to achieve robustness without losing high-resolution properties. Moreover, several commonly used numerical flux functions are implemented with the present scheme, showing the flexibility of WCNSs. The influence of variant flux functions is investigated accordingly.

For introducing the ideas of this work, the remainder of this article is organized as follows. In the next section, the fundamentals and basic equations of compact nonlinear schemes are introduced, and the proposed schemes are derived in Section 3. Section 4 presents solutions of scalar equations and the Euler equations, and concluding remarks are given in the last section.

2. Fundamentals

The governing equations of compressible flows are hyperbolic systems. Without loss of generality, the one-dimensional scalar hyperbolic conservation law can be first used to discuss numerical methods modelling compressible flows; this takes the form

$$\frac{\partial u}{\partial t} + \frac{\partial f(u)}{\partial x} = 0, \quad (1)$$

which is subject to the initial condition

$$u(x, 0) = u_0(x), \quad (2)$$

where u is the dependent variable, and $f(u)$ is the flux term. The governing equation (Eq. (1)), together with its initial condition (Eq. (2)), composes an initial-value problem (IVP), which is assumed to be well-posed in the sense that the solution u continuously depends on the initial field, and the solution is piecewise smooth with a finite number of discontinuities.

Here, Eq. (1) is discretized on an equally-spaced grid in one dimension with distance between two adjacent grid nodes denoted h . At each node i , $x_i = ih$, and $u_i = u(x_i, t)$. The characteristic velocity in Eq. (1) is $\partial f(u)/\partial u$, which is assumed to be positive, without loss of generality. Therefore, at each node, a semi-discrete solution can be constructed:

$$\left(\frac{\partial u}{\partial t}\right)_i = -\hat{f}'_i, \quad i = 1, \dots, n, \quad (3)$$

where \hat{f}'_i is the approximation to the first spatial derivative of the numerical flux function f_i .

In WCNSs, \hat{f}'_i can be approximated using a centered compact scheme Deng (2002), represented in a generic form

$$\kappa \hat{f}'_{i-1} + \hat{f}'_i + \kappa \hat{f}'_{i+1} = \frac{a_1}{h} (\tilde{f}_{i+\frac{1}{2}} - \tilde{f}_{i-\frac{1}{2}}) + \frac{a_2}{h} (\tilde{f}_{i+\frac{3}{2}} - \tilde{f}_{i-\frac{3}{2}}) + \frac{a_3}{h} (\tilde{f}_{i+\frac{5}{2}} - \tilde{f}_{i-\frac{5}{2}}), \quad (4)$$

the solution of the above equation involves tridiagonal inversions if $\kappa \neq 0$, resulting into an implicit compact scheme. An explicit formula is preferred in this work due to its low computational cost, and thus $\kappa = 0$ is set for the following discussions. The corresponding coefficients on the right hand side of Eq. (4) have values $a_1 = 75/64$, $a_2 = -25/384$, and $a_3 = 3/640$, respectively. It is worth to note that this explicit scheme is not strictly a compact scheme, but can be taken as a special case of the general WCNS. Moreover, the nonlinear interpolation to be implemented in the following work can also be used by the implicit version of Eq. (4).

Midpoint flux terms in Eq. (4) are unknown and can be usually evaluated using numerical upwind flux functions. The scalar upwind flux function is given in a generic form as

$$\tilde{f}_{i\pm\frac{1}{2}} = \frac{1}{2} \left[\left(f(u_{R,i\pm\frac{1}{2}}) + f(u_{L,i\pm\frac{1}{2}}) \right) - |\hat{a}| \left(u_{R,i\pm\frac{1}{2}} - u_{L,i\pm\frac{1}{2}} \right) \right], \quad (5)$$

where the subscripts, viz., L and R , indicate, respectively, the variables on the left- and right-hand sides of the midpoint $x_{i\pm\frac{1}{2}}$; and \hat{a} is the approximate eigenvalue of the flux Jacobian matrix. The method calculating the midpoint variables $u_{L/R,i\pm\frac{1}{2}}$ is described in the next section, which is the major concern of this work.

Once the numerical approximation \hat{f}'_i is given, temporal integration of Eq. (3) is performed using the third-order strongly stable Runge–Kutta method Gottlieb et al. (2001). Detailed discussions are omitted here, since it is beyond the scope of the present work.

3. Nonlinear interpolation strategies

For simplicity, we only consider the evaluation of variables on the left-hand side of $x_{i+\frac{1}{2}}$, i.e., $u_{L,i+\frac{1}{2}}$. The interpolations of $u_{R,i+\frac{1}{2}}$ are performed by using a symmetrical form of $u_{L,i+\frac{1}{2}}$ with minor index shift. The subscript L is thus dropped for simplicity in the discussions of the following work.

3.1. The classical WCNS-JS

For the purpose of comparison, we first introduce the classical fifth-order node-to-midpoint interpolation of WCNS-JS Deng and Zhang (2000), whereby given a five-point full stencil $S_{i+\frac{1}{2}} = \{x_{i-2}, x_{i-1}, x_i, x_{i+1}, x_{i+2}\}$, a fifth-order linear approximation of the midpoint variable can be

constructed, represented by

$$u_{i+\frac{1}{2}} = u_i + \frac{1}{128} (3u_{i-2} - 20u_{i-1} - 38u_i + 60u_{i+1} - 5u_{i+2}). \quad (6)$$

This linear approximation is also noted as the optimal fifth-order accurate interpolation, which on the other hand can be equivalently represented as a combination of three third-order polynomials, each carried out over the sub-stencil

$$S_{i+\frac{1}{2},k} = \{x_{i+k-3}, x_{i+k-2}, x_{i+k-1}\}, \quad k = 1, 2, 3. \quad (7)$$

The three third-order polynomials aforementioned can be represented generically, by using the first- and second-order derivatives, in the form of

$$u_{i+\frac{1}{2},k} = u_i(x_i + \Delta x) = u_i + u_{i,k}^{(1)}\Delta x + u_{i,k}^{(2)}\frac{\Delta x^2}{2}, \quad k = 1, 2, 3. \quad (8)$$

where $\Delta x = x_{i+\frac{1}{2}} - x_i = \frac{h}{2}$, and the derivative terms are

$$\begin{aligned} u_{i,1}^{(1)} &= \frac{1}{2h}(u_{i-2} - 4u_{i-1} + 3u_i), \\ u_{i,2}^{(1)} &= \frac{1}{2h}(u_{i+1} - u_{i-1}), \\ u_{i,3}^{(1)} &= \frac{1}{2h}(-3u_i + 4u_{i+1} - u_{i+2}), \end{aligned} \quad (9)$$

and

$$\begin{aligned} u_{i,1}^{(2)} &= \frac{1}{h^2}(u_{i-2} - 2u_{i-1} + u_i), \\ u_{i,2}^{(2)} &= \frac{1}{h^2}(u_{i-1} - 2u_i + u_{i+1}), \\ u_{i,3}^{(2)} &= \frac{1}{h^2}(u_i - 2u_{i+1} + u_{i+2}), \end{aligned} \quad (10)$$

respectively. The linear scheme in Eq. (6) is therefore expressed in an equivalent form as

$$u_{i+\frac{1}{2}} = \sum_{k=1}^3 d_k u_{i+\frac{1}{2},k}, \quad (11)$$

where the optimal weights are

$$d_1 = \frac{1}{16}, \quad d_2 = \frac{10}{16}, \quad d_3 = \frac{5}{16}. \quad (12)$$

Nonlinear weights are used to take the place of optimal weights in order to alleviate non-physical oscillations when sub-stencils are crossing discontinuities. For instance, the nonlinear weights of Jiang and Shu (1996) are given by

$$\omega_k = \frac{\alpha_k}{\sum_{k=1}^3 \alpha_k}, \quad \alpha_k = \frac{d_k}{(\beta_k + \epsilon)^2}, \quad (13)$$

where the small parameter $\epsilon = 10^{-6}$ is used to prevent division by zero, and β_k is the local smoothness indicator in the form of

$$\beta_k = \left(h u_{i,k}^{(1)} \right)^2 + \left(h^2 u_{i,k}^{(2)} \right)^2. \quad (14)$$

It has been found that the corresponding JS weight can adaptively approach 0 for a sub-stencil crossing discontinuities, thus diminishing possible numerical oscillations, and continuously approximate the optimal weight in smooth regions, therefore achieving high-order accuracy.

3.2. The multi-resolution strategy

Classical WCNSs use sub-stencils of equal-size for midpoint interpolation, as the WCNS-JS introduced in the last subsection. A multi-resolution strategy of Zhu and Shu (2018), however, makes use of one 1-point sub-stencil, one 3-point sub-stencil, and one 5-point sub-stencil for the construction of a fifth-order scheme. This strategy is employed for the midpoint interpolation in the proposed work, and its procedure is summarized as follows.

Step 1. Construct optimal linear polynomials of different degrees for the selected 1-point sub-stencil $S_{i+\frac{1}{2},1} = \{x_i\}$, 3-point sub-stencil $S_{i+\frac{1}{2},2} = \{x_{i-1}, x_i, x_{i+1}\}$, and 5-point sub-stencil $S_{i+\frac{1}{2},3} = \{x_{i-2}, x_{i-1}, x_i, x_{i+1}, x_{i+2}\}$, given by

$$\begin{aligned} q_1 &= u_i, \\ q_2 &= -\frac{1}{8}u_{i-1} + \frac{3}{4}u_i + \frac{3}{8}u_{i+1}, \\ q_3 &= \frac{3}{128}u_{i-2} - \frac{5}{32}u_{i-1} + \frac{45}{64}u_i + \frac{15}{32}u_{i+1} - \frac{5}{128}u_{i+2}. \end{aligned} \quad (15)$$

Step 2. Construct a new set of polynomials by combining the above optimal linear approximations, which will be used as a base for nonlinear convex combinations to interpolate the midpoint values. Each of the new polynomials are computed successively, and can be expressed as

$$\begin{aligned} p_1 &= q_1, \\ p_2 &= \frac{1}{\gamma_{2,2}}q_2 - \frac{\gamma_{1,2}}{\gamma_{2,2}}p_1, \\ p_3 &= \frac{1}{\gamma_{3,3}}q_3 - \frac{\gamma_{1,3}}{\gamma_{3,3}}p_1 - \frac{\gamma_{2,3}}{\gamma_{3,3}}p_2. \end{aligned} \quad (16)$$

For simplicity, the polynomial p_s for $s > 1$ can be represented in a generic form

$$p_s = \frac{1}{\gamma_{s,s}}q_s - \sum_{l=1}^{s-1} \frac{\gamma_{l,s}}{\gamma_{s,s}}p_l \quad \text{for } s = 2, 3. \quad (17)$$

Coefficient $\gamma_{l,s}$ is linear weight to be determined, and is first required to satisfy $\sum_{l=1}^s \gamma_{l,s} = 1$ and $\gamma_{s,s} \neq 0$ for $s = 2, 3$.

Choices of $\gamma_{l,s}$ are not unique. An equation for these parameters of a fifth-order scheme are provided in the work of Zhu and Shu (2018), which is based on the compromise between essentially non-oscillatory behavior near discontinuities and accuracy in smooth flow regions, given by

$$\gamma_{l,s} = \frac{\bar{\gamma}_{l,s}}{\sum_{m=1}^s \bar{\gamma}_{m,s}} \quad \text{for } l = 1, \dots, s, \quad \text{and } s = 2, 3, \quad (18)$$

where

$$\bar{\gamma}_{l,s} = 10^{l-1}. \quad (19)$$

Therefore, it can be readily determined that $\gamma_{1,2} = 1/11$, and $\gamma_{2,2} = 10/11$; $\gamma_{1,3} = 1/111$, $\gamma_{2,3} = 10/111$, and $\gamma_{3,3} = 100/111$.

Step 3. Evaluate the local smoothness indicator β_s of each sub-stencil. **Here, we follow the same recipe of the classical WCNS by Deng and Zhang (2000) for the construction of smoothness indicators, which are different than used in the WENO scheme by Jiang and Shu (1996). It is possible that this difference can affect the performance of numerical schemes. The generic form of the smoothness indicators is given by**

$$\beta_s = \sum_{n=1}^{s-1} \left(h^n u_{i,s}^{(n)} \right)^2, \quad s = 2, 3, \quad (20)$$

where $u_{i,s}^{(n)}$ denotes the (approximated) n -th derivative at x_i for each sub-stencil. More specifically, β_2 are evaluated by using

$$\begin{aligned} u_{i,2}^{(1)} &= \frac{1}{2h} (u_{i+1} - u_{i-1}), \\ u_{i,2}^{(2)} &= \frac{1}{h^2} (u_{i-1} - 2u_i + u_{i+1}), \end{aligned} \quad (21)$$

and for β_3 , derivatives are given by

$$\begin{aligned} u_{i,3}^{(1)} &= \frac{1}{12h} (u_{i-2} - 8u_{i-1} + 8u_{i+1} - u_{i+2}), \\ u_{i,3}^{(2)} &= \frac{1}{12h^2} (-u_{i-2} + 16u_{i-1} - 30u_i + 16u_{i+1} - u_{i+2}), \\ u_{i,3}^{(3)} &= \frac{1}{2h^3} (-u_{i-2} + 2u_{i-1} - 2u_{i+1} + u_{i+2}), \\ u_{i,3}^{(4)} &= \frac{1}{h^4} (u_{i-2} - 4u_{i-1} + 6u_i - 4u_{i+1} + u_{i+2}). \end{aligned} \quad (22)$$

β_1 is an exception, which is particularly computed by

$$\beta_1 = \frac{1}{\sigma^2} [\sigma_0(u_i - u_{i-1}) + \sigma_1(u_{i+1} - u_i)]^2. \quad (23)$$

Thereinto, σ , σ_0 and σ_1 are given by

$$\sigma_0 = \gamma_{0,1} \left(1 + \frac{|\zeta_0 - \zeta_1|^q}{\zeta_0 + \varepsilon} \right), \quad \sigma_1 = \gamma_{1,1} \left(1 + \frac{|\zeta_0 - \zeta_1|^q}{\zeta_1 + \varepsilon} \right), \quad \text{and} \quad \sigma = \sigma_0 + \sigma_1, \quad (24)$$

where

$$\zeta_0 = (u_i - u_{i-1})^2, \quad \zeta_1 = (u_{i+1} - u_i)^2, \quad (25)$$

$$\gamma_{0,1} = \frac{\bar{\gamma}_{0,1}}{11}, \quad \gamma_{1,1} = 1 - \gamma_{0,1}, \quad \text{and} \quad \bar{\gamma}_{0,1} = \begin{cases} 1, & \zeta_0 \geq \zeta_1 \\ 10, & \text{otherwise.} \end{cases} \quad (26)$$

The integer power exponent $q = 2$ is used for the proposed fifth-order scheme. Different values, however, are suggested for higher-order schemes as in the work Zhu and Shu (2018). The small threshold value for the reported studies was suggested as $\varepsilon = 10^{-10}$ to avoid the influence of round-off error.

Step 4. Calculate the nonlinear weights for the following convex combinations of polynomials reconstructed in Step 2. Inspired by the form of nonlinear weights of Borges et al. (2008), an absolute difference among local smoothness indicators is defined as

$$\tau_3 = \left(\frac{|\beta_3 - \beta_1| + |\beta_3 - \beta_2|}{2} \right)^2. \quad (27)$$

The nonlinear weights are then given by

$$\omega_k = \frac{\alpha_k}{\sum_{m=1}^3 \alpha_m}, \quad \alpha_k = \gamma_{k,3} \left(1 + \frac{\tau_3}{\varepsilon + \beta_k} \right), \quad k = 1, 2, 3. \quad (28)$$

Here, $\varepsilon = 10^{-10}$ is also used to avoid the denominator becoming zero. Linear weights $\gamma_{k,3}$ were given in Step 2.

Step 5. Perform convex combinations of polynomials obtained in Eq. (16) by using nonlinear weights given in Eq. (28) such that

$$u_{i+\frac{1}{2}} = \sum_{m=1}^3 \omega_m p_m. \quad (29)$$

Without difficult derivations, one can readily see that if the full stencil is smooth enough, all local smoothness indicators satisfy $\beta_k \approx 0$ as a consequence, further yielding $\omega_k = \gamma_{k,3}$. The fifth-order optimal polynomials q_3 is then perfectly recovered in Eq. (29), so is the third-order linear scheme q_2 when the 1-point sub-stencil and 3-point sub-stencil are both smooth, yet the 5-point sub-stencil is regarded oscillatory. Similarly, $u_{i+\frac{1}{2}}$ can further degrade down to first-order accurate if the 3- and 5-point sub-stencils are both oscillatory. For this reason, numerical robustness is obtained as expected by this method when dealing with severe discontinuities.

4. Numerical results and analyses

A variety of canonical problems are simulated to assess the performance of the present method. The one-dimensional linear advection equation, the one-dimensional inviscid Burgers' equation and the Euler equations of gas dynamics are used as model equations in this section. We note that a CFL number equal to 0.4 has been used in computing all of the test cases reported herein, except that in the scalar problem, the CFL numbers are sufficiently small to achieve temporally stable and converged results. A different number, i.e. CFL= 0.1, is also used for the verification of high-order accuracy in the simulation of the 2D isentropic vortex propagation problem to avoid possible spatial resolution deterioration caused by the temporal scheme. For each test case, the solution of the multi-resolution WENO scheme Zhu and Shu (2018) using the Lax-Friedrichs splitting, is used as a reference for the comparison purpose.

4.1. Approximate dispersion relation

Before doing the case-by-case investigation, a numerical error metric for smooth wave propagation is presented at first. Dispersion and dissipation properties of the numerical scheme proposed in this work, denoted as WCNS-MR, are evaluated by using the approximate dispersion relation (ADR) analysis of Pirozzoli (2006). We also provide the spectral behaviors of the multi-resolution WENO scheme, denoted as WENO-MR, for the comparison purpose. The ADR analysis evaluates the dissipation and dispersion errors of numerical schemes in wave-number space by solving a linear advection equation with a smooth sinusoidal initial condition including different Fourier modes supported on a given grid Pirozzoli (2006). A reduced wave-number ξ (normalized to lie in the interval $[0, \pi]$) is defined for all supported modes, and its real (ξ_R) and imaginary (ξ_I) parts represent dispersion and dissipation properties, respectively, for the numerical schemes being evaluated.

Figure 1 shows that the proposed WCNS-MR yields better dispersion properties compared with the WENO-MR scheme, in a wide range of wave-numbers. The difference is more significant within the intermediate wave-number regime. In the high wave-number regime, larger dissipation error of WCNS-MR is found, compared with WENO-MR. However, this minor large dissipation for the high wave-number mode is not necessarily a bad feature since it helps to damp the increased phase error therein. In general, the present method shows comparable or better performance in resolving linear smooth waves of high frequency.

4.2. Scalar equations

4.2.1. Linear advection problem

The one-dimensional Gaussian pulse advection problem of Shu and Osher (1989), is used to assess the order of accuracy of the proposed scheme when solutions are smooth. This problem is governed by the linear advection equation

$$\frac{\partial u}{\partial t} + \frac{\partial u}{\partial x} = 0, \quad x \in [0, 1], \quad (30)$$

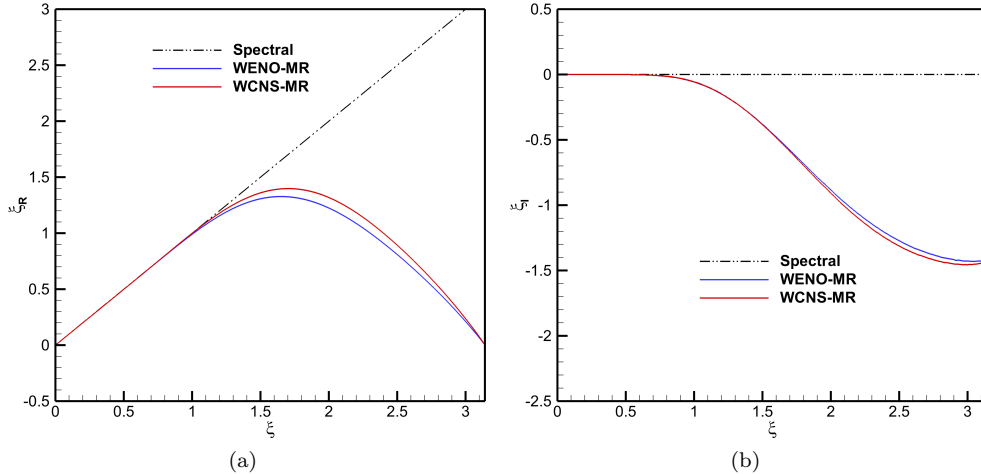


Figure 1.: Approximate dispersion and dissipation properties of various fifth-order schemes; (a) dispersion, and (b) dissipation.

with periodic boundary conditions and initial condition

$$u(x, 0) = e^{-300(x-x_c)^2}, \quad x_c = 0.5. \quad (31)$$

Temporal integration is performed up to $t = 1$, corresponding to one period of the single wave propagation in time. Uniformly-spaced grids are progressively refined by a factor of two from the coarsest grid of $N = 51$ points. As noted above, the numerical simulation on each grid is conducted using sufficiently small time steps so as to achieve temporally converged results.

Table 1, Table 2 and Fig. 2 illustrate numerical errors and convergence rates of the various numerical schemes used. The order of accuracy of WENO-MR and WCNS-MR achieves approximately fifth-order, during the mesh refinement. The L^1 - and L^∞ -errors of WCNS-MR, however, coincide with those of the background linear (compact) scheme as the meshes are progressively refined, demonstrating its improved resolution compared with the WENO-MR scheme.

Table 1.: L^1 -error and convergence rates of fifth-order schemes solving the linear advection equation at $t = 1$.

| N | Linear5 | | WENO-MR | | WCNS-MR | |
|------|----------|-------|----------|-------|----------|-------|
| | Error | Order | Error | Order | Error | Order |
| 51 | 6.82E-03 | * | 9.50E-03 | * | 9.14E-03 | * |
| 101 | 3.31E-04 | 4.36 | 9.70E-04 | 3.29 | 1.23E-03 | 2.89 |
| 201 | 1.10E-05 | 4.91 | 2.42E-05 | 5.32 | 2.55E-05 | 5.60 |
| 401 | 3.48E-07 | 4.99 | 4.94E-07 | 5.61 | 3.48E-07 | 6.19 |
| 801 | 1.09E-08 | 5.00 | 1.55E-08 | 4.99 | 1.09E-08 | 5.00 |
| 1601 | 3.41E-10 | 5.00 | 4.85E-10 | 5.00 | 3.41E-10 | 5.00 |

4.2.2. Inviscid Burgers' equation

The one-dimensional inviscid Burgers' equation is used to assess the order of accuracy of the nonlinear schemes being investigated when they are applied to solving a nonlinear scalar equation. The governing equation is

$$\frac{\partial u}{\partial t} + \frac{1}{2} \frac{\partial u^2}{\partial x} = 0, \quad x \in [0, 2], \quad (32)$$

Table 2.: L^∞ -error and convergence rates of fifth-order schemes solving the linear advection equation at $t = 1$.

| N | Linear5 | | WENO-MR | | WCNS-MR | |
|------|----------|-------|----------|-------|----------|-------|
| | Error | Order | Error | Order | Error | Order |
| 51 | 5.22E-02 | * | 9.09E-02 | * | 8.95E-02 | * |
| 101 | 3.30E-03 | 3.98 | 1.68E-02 | 2.43 | 2.27E-02 | 1.98 |
| 201 | 1.16E-04 | 4.83 | 6.50E-04 | 4.69 | 8.00E-04 | 4.83 |
| 401 | 3.69E-06 | 4.97 | 6.84E-06 | 6.57 | 5.91E-06 | 7.08 |
| 801 | 1.16E-07 | 4.99 | 1.74E-07 | 5.29 | 1.29E-07 | 5.52 |
| 1601 | 3.63E-09 | 5.00 | 5.22E-09 | 5.06 | 3.71E-09 | 5.12 |

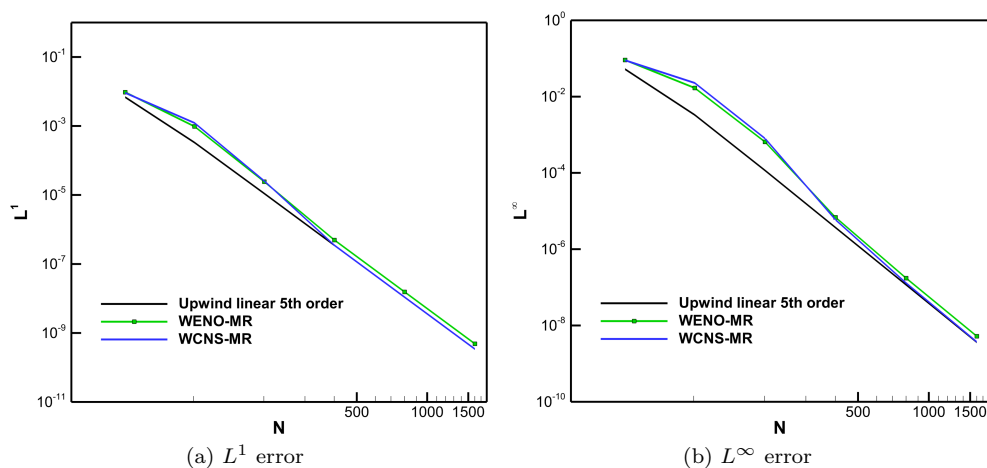


Figure 2.: Convergence rates of fifth-order schemes at $t = 1$ for L^1 - and L^∞ -errors in solutions to the linear advection equation.

with periodic boundary conditions and initial condition

$$u(x, 0) = \frac{1}{2} + \sin(\pi x). \quad (33)$$

The exact solution is computed by solving the derived general characteristic relation given in Harten et al. (1987). The solution is smooth for $0 \leq t < 1/\pi$. L^1 - and L^∞ -errors and convergence rate of each scheme at $t = 0.2$ are presented in Table 3 and Table 4, and also shown in Fig. 3. Perfect agreement can be found for WCNS-MR and the underlying fifth-order linear scheme as the mesh is progressively refined, indicating the optimal linear (compact) schemes are recovered by the proposed scheme. WENO-MR yields results with formal order of accuracy higher than five. However, this is because that the WENO-MR scheme produces large numerical errors on coarse meshes.

Table 3.: L^1 -error and convergence rates of fifth-order schemes solving the 1-D inviscid Burgers equation at $t = 0.2$.

| N | Linear5 | | WENO-MR | | WCNS-MR | |
|-----|----------|-------|----------|-------|----------|-------|
| | Error | Order | Error | Order | Error | Order |
| 21 | 5.89E-04 | * | 2.49E-03 | * | 1.67E-03 | * |
| 41 | 7.72E-05 | 2.93 | 2.18E-04 | 3.51 | 1.43E-04 | 3.54 |
| 81 | 3.33E-06 | 4.53 | 7.34E-06 | 4.89 | 3.48E-06 | 5.37 |
| 161 | 1.18E-07 | 4.82 | 1.90E-07 | 5.27 | 1.18E-07 | 4.88 |
| 321 | 3.86E-09 | 4.93 | 4.77E-09 | 5.31 | 3.86E-09 | 4.93 |

Table 4.: L^∞ -error and convergence rates of fifth-order schemes solving the 1-D inviscid Burgers equation at $t = 0.2$.

| N | Linear5 | | WENO-MR | | WCNS-MR | |
|-----|----------|-------|----------|-------|----------|-------|
| | Error | Order | Error | Order | Error | Order |
| 21 | 3.94E-03 | * | 1.06E-02 | * | 1.00E-02 | * |
| 41 | 9.98E-04 | 1.98 | 2.95E-03 | 1.84 | 1.00E-03 | 3.32 |
| 81 | 9.06E-05 | 3.46 | 1.34E-04 | 4.46 | 9.06E-05 | 3.47 |
| 161 | 3.24E-06 | 4.81 | 4.49E-06 | 4.90 | 3.24E-06 | 4.81 |
| 321 | 1.04E-07 | 4.96 | 1.16E-07 | 5.27 | 1.04E-07 | 4.96 |

4.3. Euler equations

For the gas dynamic problems simulated here, the governing equations are 2D Euler equations, which are introduced as follows, and 1D Euler equations can be then obtained by a straightforward simplification, i.e. assuming $v = 0$. The equations are

$$\begin{aligned} \frac{\partial \rho}{\partial t} + \frac{\partial(\rho u)}{\partial x} + \frac{\partial(\rho v)}{\partial y} &= 0, \\ \frac{\partial(\rho u)}{\partial t} + \frac{\partial(\rho u^2)}{\partial x} + \frac{\partial(\rho uv)}{\partial y} &= -\frac{\partial p}{\partial x}, \\ \frac{\partial(\rho v)}{\partial t} + \frac{\partial(\rho uv)}{\partial x} + \frac{\partial(\rho v^2)}{\partial y} &= -\frac{\partial p}{\partial y}, \\ \frac{\partial E}{\partial t} + \frac{\partial(uE)}{\partial x} + \frac{\partial(vE)}{\partial y} &= -\frac{\partial(up)}{\partial x} - \frac{\partial(vp)}{\partial y}. \end{aligned}$$

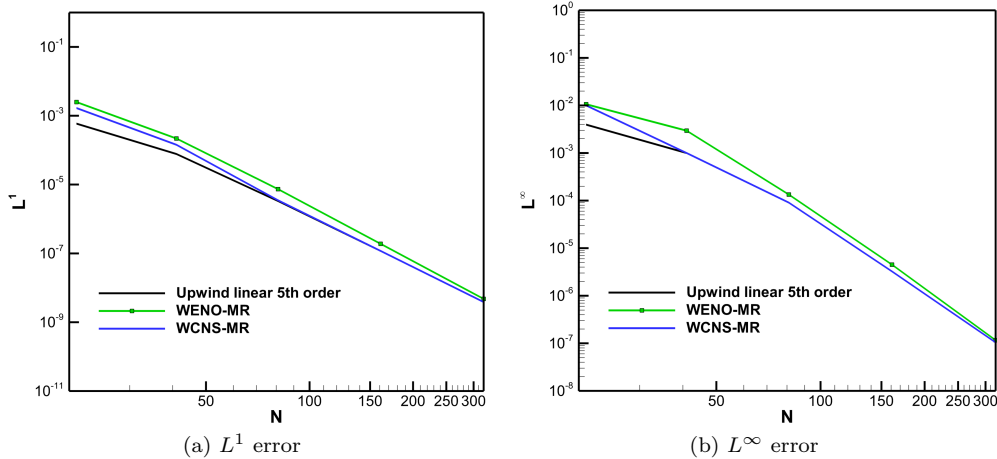


Figure 3.: Convergence rates of fifth-order schemes at $t = 0.2$ for L^1 - and L^∞ -errors in solutions to the one-dimensional inviscid Burgers' equation.

where $E = e + \frac{1}{2}u^2$ is the total energy per unit mass, and e is internal energy. The dependent variables are related through the perfect gas equation of state given by $p = (\gamma - 1)\rho e$ with $\gamma = 1.4$, except for the Rayleigh-Taylor instability problem ($\gamma = \frac{5}{3}$), thus closing the Euler equations system.

Node-to-midpoint interpolation is performed on characteristic fields to alleviate spurious oscillations Deng and Zhang (2000). While solving the Euler equations, a robust and high-resolution numerical flux scheme is also an essential component of the numerical solver Zhang et al. (2016, 2017); Qu et al. (2018). For high-order methods the numerical flux schemes can be influential for the overall robustness and resolution Drikakis and Tsangaris (1993); Wang et al. (2016). Here, three classical schemes, viz. the Rusanov scheme Rusanov (1961), van Leer scheme van Leer (1982) and HLL scheme Harten et al. (1983), are employed for the computation of numerical fluxes. The multi-resolution WENO scheme is denoted as WENO-MR-LF in the following work.

4.3.1. Sod and Lax shock tube problems

Riemann initial-value problems of Sod (1978) and Lax (1954) are used to evaluate the shock-capturing capability of the proposed scheme employing discretization of the 1-D Euler equations.

The Sod shock tube problem involves a right-moving shock of Mach number 1.7, while for the Lax shock tube problem, the right-moving shock has Mach number 2.0. Initial conditions for the Sod problem are

$$(\rho, u, p) = \begin{cases} (1, 0, 1) & x \in [0, 0.5], \\ (0.125, 0, 0.1) & x \in (0.5, 1], \end{cases} \quad (34)$$

and the results at $t = 0.2$ are given by solving the problem on an evenly-distributed grid of $N = 101$ points.

Density and velocity distributions obtained by all schemes are close to each other, as shown in Fig. 4. The results are free of spurious oscillations near the shock both for density and velocity profiles, and the shock-capturing capability of all WCNS-MRs is somewhat shown to be better than the WENO-MR scheme.

Initial conditions for the Lax shock-tube problem are

$$(\rho, u, p) = \begin{cases} (0.445, 0.698, 3.528) & x \in [0, 0.5], \\ (0.5, 0, 0.571) & x \in (0.5, 1]. \end{cases} \quad (35)$$

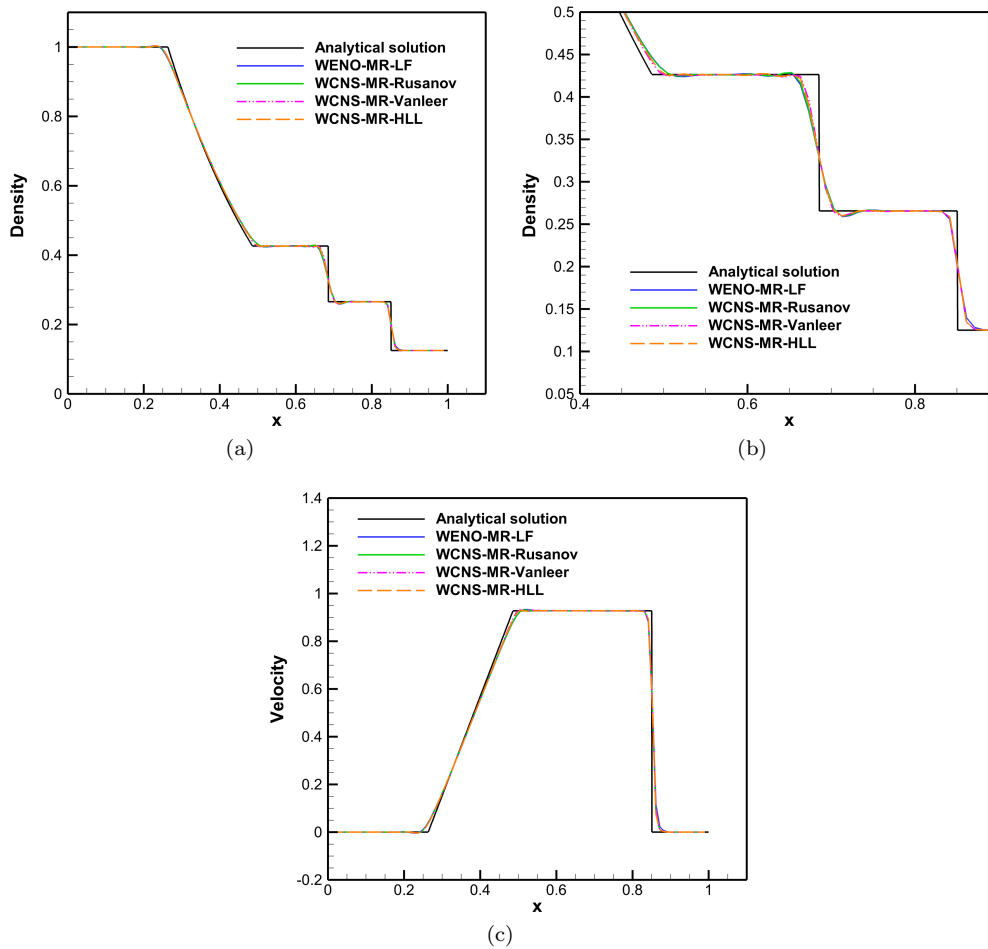


Figure 4.: Numerical and exact solutions of the Sod problem at $t = 0.2$; (a) density, (b) zoom in of density, (c) velocity.

This case is also simulated on an evenly distributed grid of $N = 101$ points, and the density and velocity distributions at $t = 0.14$ are shown in Fig. 5.

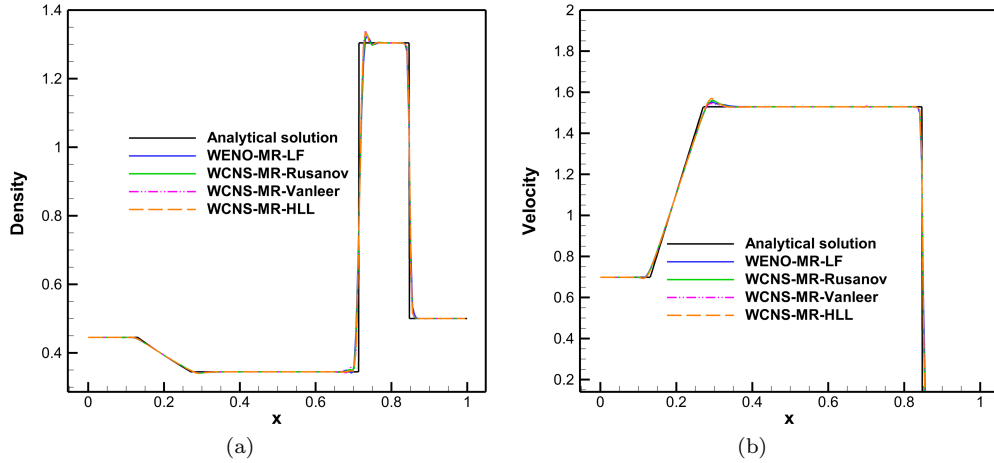


Figure 5.: Numerical and exact solutions of the Lax problem at $t = 0.14$; (a) density, and (b) velocity.

Overall, the solutions of all nonlinear schemes are rather close and reasonably decent. Again, the shock profile is sharply captured in the Lax problem by all schemes used. Minor overshoot is noticeable in the density profile near the contact discontinuity, and in the velocity distribution near the tail of the expansion fan; but such overshoots, are considered to be acceptable in this work since similar behaviors are also seen in various other high-order schemes.

4.3.2. Shock/density-wave interaction of Osher and Shu

The shock/density-wave interaction problem of Shu and Osher (1989) is characterized by a right-moving shock wave of Mach number 3 interacting with high-frequency sine waves in the density field. This problem is initialized by

$$(\rho, u, p) = \begin{cases} (3.857, 2.629, 10.333), & x \in [0, 1], \\ (1 + 0.2\sin(5x), 0, 1), & x \in (1, 10]. \end{cases} \quad (36)$$

A multi-scale wave structure evolves after the shock wave interacts with the oscillating density wave, and both shock-capturing and wave-resolution capabilities are evaluated for the methods considered herein via this problem. This case is run on a grid of $N = 201$ points which are uniformly distributed, and the final computing time is $t = 1.8$. Since there is no theoretical solution for this problem, a fine-grid numerical solution via the WENO-MR on a grid of $N = 2001$ points is used as a reference.

As shown in Fig. 6, all WCNS-MRs produce considerably better resolved density waves behind the shock wave compared with WENO-MR-LF. Solutions among WCNS-MRs agree with each other closely, implying that the multi-scale wave structure in this case is not sensitive to the type of flux functions used for WCNS-MR.

4.3.3. Propagation of a strong vortex in two dimensions

A test case involving an isentropic vortex propagating at a supersonic Mach number Balsara and Shu (2000) is used to evaluate the high-order accuracy of the numerical schemes considered in 2D. The initial flow state properties are carefully manipulated in the domain $[-20, 20] \times [-20, 20]$ so that the vortex propagates along the diagonal of the domain. The mean flow properties

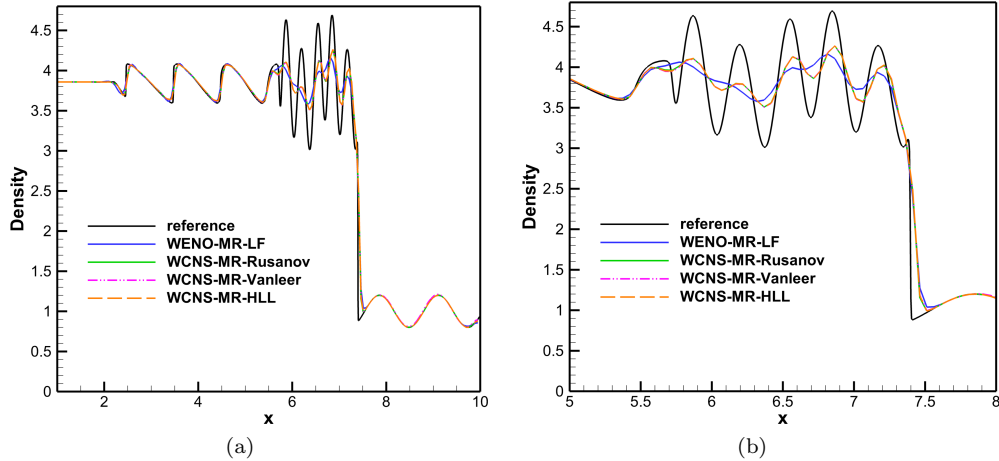


Figure 6.: Shock/density-wave interaction problem; numerical solutions and the exact solution at $t = 1.8$; (a) full spatial domain, and (b) zoom in on high-amplitude region.

are specified initially as $(\rho, u, v, p) = (1, 1, 1, 1)$ for the whole computational domain, and the perturbation variables which define the vortex are given by

$$\left\{ \begin{array}{l} \tilde{u} = -\frac{y\epsilon}{2\pi}e^{0.5(1-r^2)} \\ \tilde{v} = \frac{x\epsilon}{2\pi}e^{0.5(1-r^2)} \\ \tilde{T} = -\frac{(\gamma-1)\epsilon^2}{8\gamma\pi^2}e^{(1-r^2)} \\ \tilde{S} = 0 \end{array} \right. , \quad (37)$$

where it can be found that the superposition is performed through perturbations on velocity (u, v) , temperature T , given by $T = p/\rho$, and entropy S , defined as $S = (p/\rho^\gamma)$ in this specific case. In addition, $r^2 = x^2 + y^2$, and the vortex strength is determined by $\epsilon = 5$.

Computations are run up to $t = 2$, and in such a case, the moving vortex has not reached any boundaries of the computational domain. Fixed flow state properties $(\rho, u, v, p) = (1, 1, 1, 1)$ can be therefore used for boundary conditions. As aforementioned, CFL= 0.1 is used for the time-stepping. Tables 5 and 6 show L^1 , and L^∞ norm errors of the numerical solutions, respectively, along with their convergence rates with respect to a sequence of progressively refined grids. All WCNS-MRs exhibit better convergence rates than the WENO-MR scheme. WCNS-MRs also yield more accurate solutions than the WENO-MR scheme on the same grid. For instance, the solution is nearly one order of magnitude more accurate on the finest mesh when using WCNS-MRs. Among three WCNS-MRs, WCNS-MR-Rusanov is less accurate than the other two schemes. The resolutions of WCNS-MR-HLL and WCNS-MR-Vanleer, however, are close.

Table 5.: L^1 -error and convergence rate of fifth-order schemes simulating the propagation of a strong vortex in 2D ($t = 2$).

| N | WENO-MR-LF | | WCNS-MR-Rusanov | | WCNS-MR-HLL | | WCNS-MR-Vanleer | |
|-----|------------|-------|-----------------|-------|-------------|-------|-----------------|-------|
| | Error | Order | Error | Order | Error | Order | Error | Order |
| 81 | 2.45E-04 | * | 1.37E-04 | * | 1.33E-04 | * | 1.38E-04 | * |
| 161 | 2.30E-05 | 3.41 | 1.29E-05 | 3.40 | 1.01E-05 | 3.72 | 1.05E-05 | 3.71 |
| 321 | 1.29E-06 | 4.16 | 4.27E-07 | 4.92 | 3.34E-07 | 4.91 | 3.47E-07 | 4.92 |
| 641 | 2.47E-08 | 5.70 | 9.37E-09 | 5.51 | 6.16E-09 | 5.76 | 5.63E-09 | 5.95 |

Table 6.: L^∞ -error and convergence rate of fifth-order schemes simulating the propagation of a strong vortex in 2D ($t = 2$).

| N | WENO-MR-LF | | WCNS-MR-Rusanov | | WCNS-MR-HLL | | WCNS-MR-Vanleer | |
|-----|------------|-------|-----------------|-------|-------------|-------|-----------------|-------|
| | Error | Order | Error | Order | Error | Order | Error | Order |
| 81 | 7.77E-02 | * | 4.14E-02 | * | 3.99E-02 | * | 3.88E-02 | * |
| 161 | 1.08E-02 | 2.84 | 5.73E-03 | 2.85 | 4.74E-03 | 3.07 | 6.60E-03 | 2.55 |
| 321 | 8.46E-04 | 3.68 | 2.31E-04 | 4.63 | 2.49E-04 | 4.25 | 3.73E-04 | 4.15 |
| 641 | 2.50E-05 | 5.08 | 2.47E-06 | 6.55 | 1.91E-06 | 7.03 | 1.93E-06 | 7.59 |

4.3.4. Two-dimensional Riemann problems

In this section, the configurations 3 and 6 out of 19 2-D Riemann problems used by Lax and Liu (1998) are employed to evaluate performance of the currently investigated numerical schemes. In particular, these two configurations are characterized by rich small scales in the flow fields, and thus are specifically chosen to evaluate the ability of the proposed numerical schemes to resolve fine flow structures. These 2-D Riemann problems are widely-solved canonical problems in the present context, analogous to the 1-D Sod shock tube problem of the previous section.

Configuration 3

Initial conditions for configuration 3 are given by

$$(\rho, u, v, p) = \begin{cases} (1.5, 0, 0, 1.5) & (x, y) \in [\frac{1}{2}, 1] \times [\frac{1}{2}, 1], \\ (0.5323, 1.206, 0, 0.3) & (x, y) \in [0, \frac{1}{2}] \times [\frac{1}{2}, 1], \\ (0.138, 1.206, 1.206, 0.029) & (x, y) \in [0, \frac{1}{2}] \times [0, \frac{1}{2}], \\ (0.5323, 0, 1.206, 0.3) & (x, y) \in [\frac{1}{2}, 1] \times [0, \frac{1}{2}], \end{cases} \quad (38)$$

and the boundary conditions are

$$\begin{aligned} \frac{\partial \mathbf{u}(x, y, t)}{\partial x} &= 0, & x = 0, 1, & \quad \forall y, t, \\ \frac{\partial \mathbf{u}(x, y, t)}{\partial y} &= 0, & y = 0, 1, & \quad \forall x, t, \end{aligned} \quad (39)$$

where the vector of primitive variables is given by $\mathbf{u} = (\rho, u, v, p)^T$. Ghost nodes are used adjacent to boundary nodes of the domain to implement these conditions. It should be noted that computations are terminated before the shock structures interact with boundaries, and thus the discussion will focus on the central part of the flow field.

Solutions obtained on a mesh of 1024^2 grid points with uniform spacing by WCNS-MRs and WENO-MR at $t = 0.3$ are shown in Fig 7. All WCNS-MRs capture more vortices along contact lines than does the WENO-MR-LF scheme. The solutions computed using variant flux functions for WCNS-MRs, however, are different. In particular, the WCNS-MR-Vanleer resolves a few small features not seen in the other figures.

Without physical results for comparisons, one must question whether these flow structures actually represents physics. In fact, Shi et al. (2003) suggested that during a mesh refinement slip lines usually are non-physical and depend on numerical schemes being used. However, these simulations are important for identifying the magnitude of numerical viscosities; and the small numerical viscosity indicated by these delicate structures in the flow field is a necessity to guarantee that the physical viscosity in Navier–Stokes simulation is not overwhelmed. **Moreover, in this numerical case, expected symmetries are lost in all solutions. Similar behaviors were also found in references Shi et al. (2003); Zhao et al. (2018). A thorough investigation into the occurrence of symmetry breaking was carried out by Fleischmann et al. (2019) in their recent work. They demonstrated that the asymmetric flow behavior is mainly triggered by the floating-point truncation error. Several useful strategies were reported to improve the CFD code**

with symmetry preserving property. With the consistent floating-point arithmetic implemented, symmetry of the flow state variables can be recovered both in two and three dimensions.

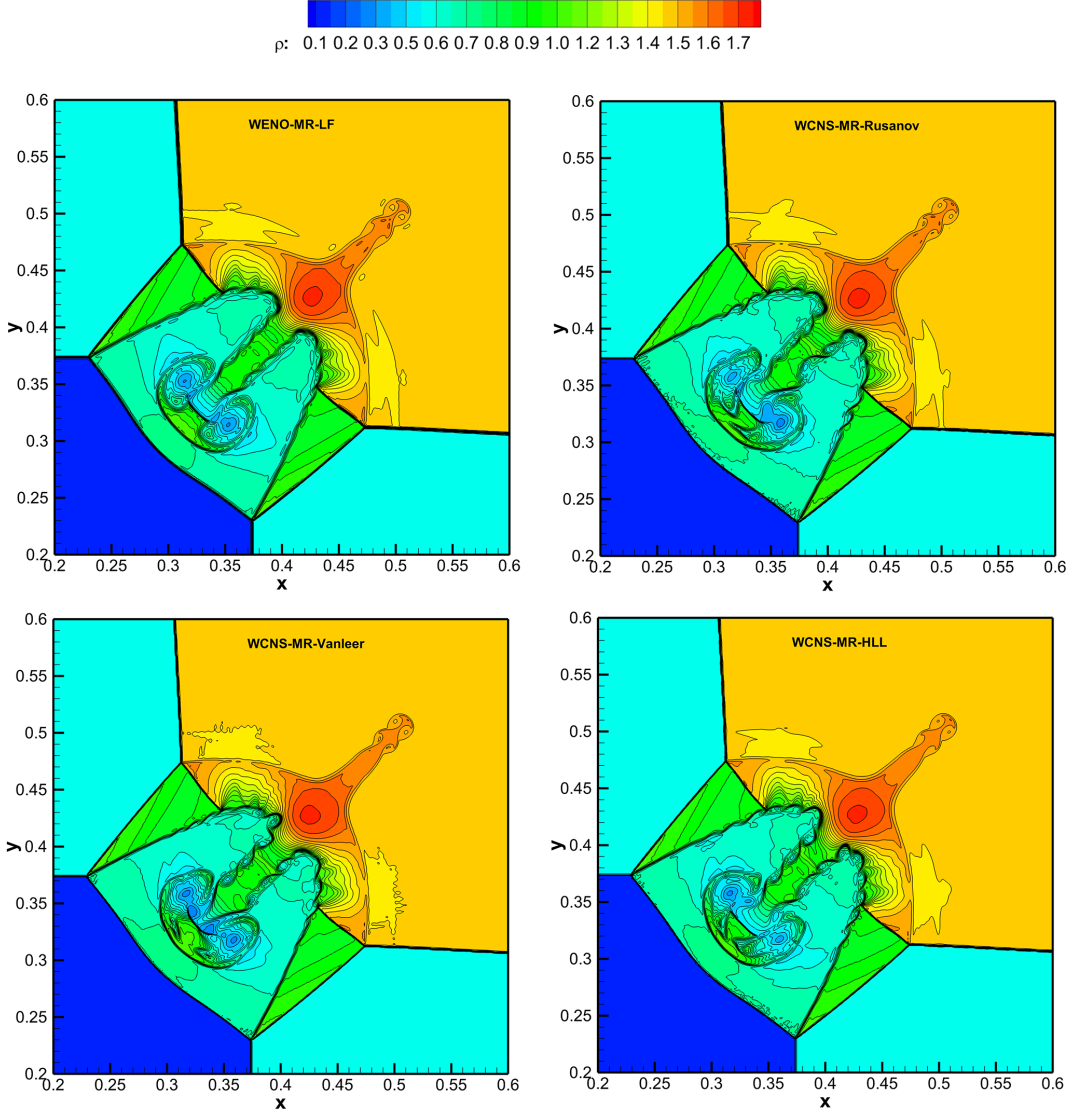


Figure 7.: Configuration 3 of 2-D Riemann problems in Lax and Liu (1998) computed on a grid of 1024×1024 points; 30 density contour lines ranging from 0.1 to 1.8 at $t = 0.3$.

Configuration 6

The equations of motion are the same as those used for configuration 3, the 2-D Euler equations, but now with initial conditions given by

$$(\rho, u, v, p) = \begin{cases} (1, 0.75, -0.5, 1) & (x, y) \in [\frac{1}{2}, 1] \times [\frac{1}{2}, 1], \\ (2, 0.75, 0.5, 1) & (x, y) \in [0, \frac{1}{2}] \times [\frac{1}{2}, 1], \\ (1, -0.75, 0.5, 1) & (x, y) \in [0, \frac{1}{2}] \times [0, \frac{1}{2}], \\ (3, -0.75, -0.5, 1) & (x, y) \in [\frac{1}{2}, 1] \times [0, \frac{1}{2}], \end{cases} \quad (40)$$

and the boundary conditions are the same as in the preceding test case.

Results obtained by using WENO-MR-LF, WCNS-MR-Rusanov, WCNS-MR-Vanleer and WCNS-MR-HLL on a uniform mesh of 1024^2 grid points at $t = 0.3$ are shown in Fig. 8. All WCNS-MRs resolve abundant small-scale flow structures along contact lines in the first and third quadrants. In the second quadrant, however, several small features along the contact

line are better captured by the WENO-MR-LF scheme, which are not seen in the solutions of WCNS-MR-Rusanov and WCNS-MR-HLL. Again, similar to the findings for the previous configuration, noticeable differences can be seen by comparing all results of WCNS-MRs in this test case—probably due to different numerical dissipation.

In the absence of physical results or demonstrably accurate simulations, we do not discuss the physical correctness of the results here. So is only numerical, as has been noted by various other investigations.

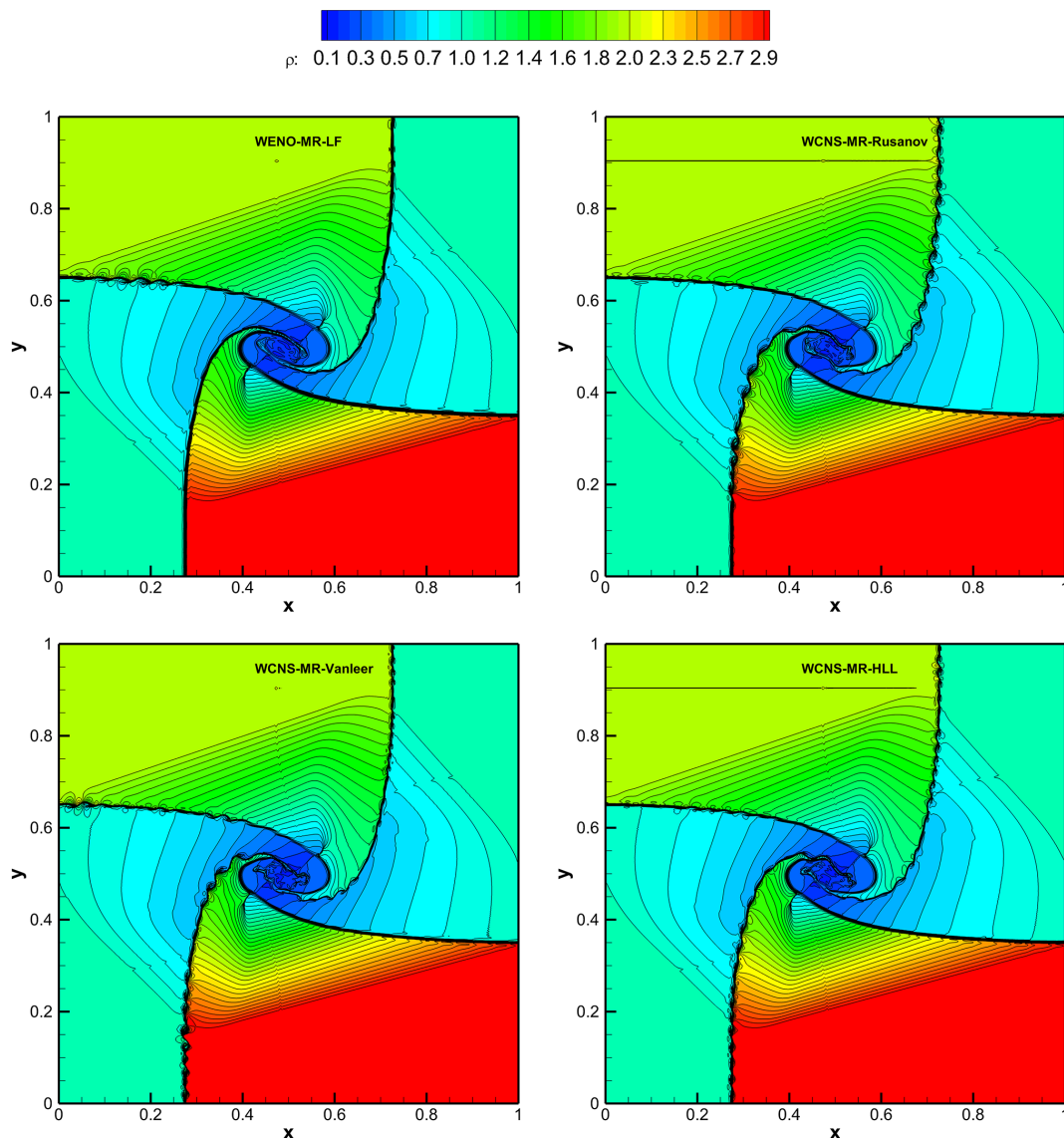


Figure 8.: Configuration 6 of 2-D Riemann problems in Lax and Liu (1998) computed on a grid of 1024×1024 points; 40 density contour lines ranging from 0.1 to 2.9 at $t = 0.3$.

4.3.5. *Rayleigh–Taylor instability*

The Rayleigh–Taylor instability problem containing both discontinuities and complex vortex structures, has been widely studied, experimentally and computationally, and it is used here as a final example for examining performance of the presently-studied methods. Again, the 2-D Euler equations comprise the basic mathematical model. In the present case, initial conditions

are given by

$$(\rho, u, v, p) = \begin{cases} (2, 0, -0.025 a \cos(8\pi x), 1 + 2y) & (x, y) \in [0, 0.25] \times [0, 0.5], \\ (1, 0, -0.025 a \cos(8\pi x), y + 3/2) & (x, y) \in [0, 0.25] \times [0.5, 1], \end{cases} \quad (41)$$

where a is the speed of sound, given by $a = \sqrt{\gamma p / \rho}$ and a different $\gamma = \frac{5}{3}$ is used for this specific case. Reflecting boundary conditions are imposed at the left- and right-hand sides of the domain; i.e., velocity u adjacent to boundary nodes is assigned the value of corresponding image nodes with sign reversed, and ρ , v , and p are straightforwardly assigned. Constant boundary conditions are given for the top and bottom sides, expressed as

$$(\rho, u, v, p) = \begin{cases} (1, 0, 0, 2.5) & y = 1, \quad \forall t, x, \\ (2, 0, 0, 1) & y = 0, \quad \forall t, x. \end{cases} \quad (42)$$

Two source terms, ρ and ρv , are added to the right-hand side of the third and the fourth equations, respectively, of the 2-D Euler system given at the beginning of this subsection, as done by Shi et al. (2003), among others. (Note: this does not correctly adhere to dimensional consistency of terms in the equations of motion, so any correspondence with actual physics would be accidental. Moreover, the Rayleigh–Taylor problem is 3D, so again, not much actual physics can be expected from these simulations, but only the numerical dissipation properties are investigated.) **A uniformly distributed mesh of 128×512 grid points is used. Density profiles at the final time $t = 1.95$, computed using the WENO-MR, and three WCNS-MR techniques, are shown in Fig. 9.**

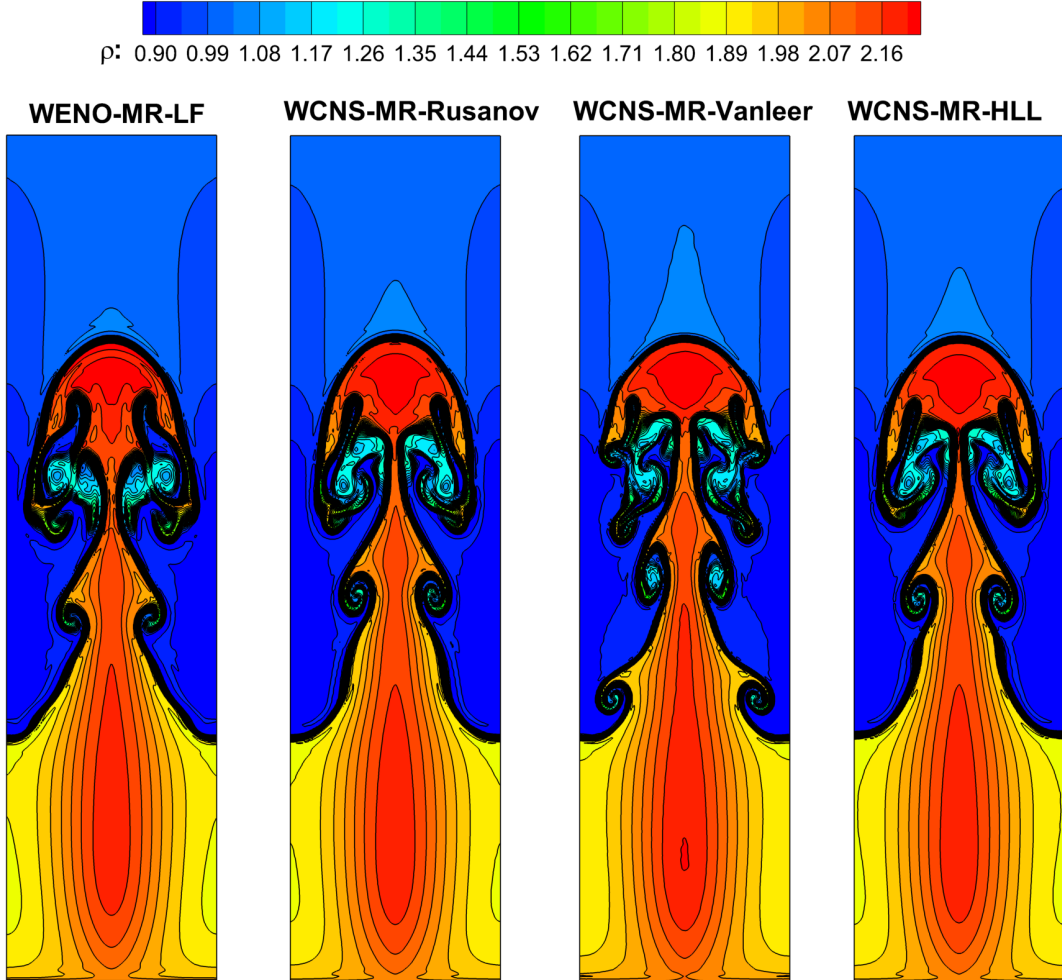


Figure 9.: Rayleigh–Taylor instability problem; 30 density contour lines ranging from 0.9 to 2.2.

Overall, WENO-MR, WCNS-MR-Rusanov, and WCNS-MR-HLL obtain similar flow structures. In the solution of WCNS-MR-Vanleer, a unique second pair of vortices rolling up along the slip lines, and more complex flow structures in the “mushroom cap” region are resolved. Moreover, symmetric density profiles are produced with all methods, as should be expected. It is worth to note again, that for this problem, a more accurate Riemann solver would be quite helpful for improving resolution of the present methods, as investigated by San and Kara (2015) for a somewhat different problem.

Moreover, in Table 7, we provide the comparison of CPU timing per time step using variant fifth-order schemes in this test case. In general, the computing time is close, since WCNS-MRs use an explicit form of Eq. 4, which does not require the time consuming tridiagonal inversion. This insignificant difference between WENO-MR and WCNS-MRs can also be changed by improving the coding performance of each scheme and the solver.

Table 7.: CPU timing (in seconds) per time step using variant fifth-order schemes in the Rayleigh–Taylor instability problem.

| Grid size | WENO-MR-LF | WCNS-MR-Rusanov | WCNS-MR-HLL | WCNS-MR-Vanleer |
|-----------|------------|-----------------|-------------|-----------------|
| 128× 512 | 0.319 | 0.313 | 0.325 | 0.297 |

5. Conclusions

Following the fundamental concept of WCNSs, a new multi-resolution strategy is introduced to construct the nonlinear interpolation procedure of WCNSs using three nested central spatial sub-stencils. The nonlinear interpolation still uses the convex combination concept of WENO schemes, but the strategy of using sub-stencils of equal-width is abandoned, and thus allowing the present scheme to gradually reduce the order of accuracy if discontinuous solution occurs. In fact, the proposed scheme can degrade to first-order interpolation for a closely located severe discontinuity. Therefore, strong robustness can be guaranteed in such a case. Moreover, as shown in the test cases above, high-resolution has been achieved by the proposed scheme both in capturing shocks and resolving complex flow structures.

In the present work, we also exploit one of the advantages of WCNSs, i.e., the flexibility of using different numerical flux functions. While the type of flux functions does not seem to affect the specific multi-scale wave structure of shock/density-wave interaction problem, the rich small scales in the 2D test cases are sensitive to the flux function selected. The key may be the capability of resolving different wave structures governed by the Euler equations, and thus it is favored to use such a high-resolution numerical flux scheme.

In conclusion, due to the advantages mentioned above, the proposed scheme is a promising alternative solution, which possesses high-resolution and low-dissipation properties, for simulating compressive flows with discontinuities.

Acknowledgments

This work was financially supported by the project of National Numerical Wind Tunnel (No. NNW2019ZT5-B15), and partially supported by the open fund from the State Key Laboratory of Aerodynamics (No. SKLA20180302).

References

Z. Wang, K. Fidkowski, R. Abgrall, F. Bassi, D. Caraeni, A. Cary, H. Deconinck, R. Hartmann, K. Hillewaert, H. Huynh, N. Kroll, G. May, P.-O. Persson, B. van Leer, M. Visbal, High-order CFD methods:

- current status and perspective, *Int. J. Numer. Meth. Fluids* 72 (8) (2013) 811–845, ISSN 1097-0363.
- S. K. Lele, Compact finite difference schemes with spectral-like resolution, *Journal of Computational Physics* 103 (1) (1992) 16 – 42, ISSN 0021-9991, .
- E. Johnsen, J. Larsson, A. V. Bhagatwala, W. H. Cabot, P. Moin, B. J. Olson, P. S. Rawat, S. K. Shankar, B. Sjögren, H. Yee, X. Zhong, S. K. Lele, Assessment of high-resolution methods for numerical simulations of compressible turbulence with shock waves, *Journal of Computational Physics* 229 (4) (2010) 1213 – 1237, ISSN 0021-9991, .
- K. Ritos, I. W. Kokkinakis, D. Drikakis, Performance of high-order implicit large eddy simulations, *Computers & Fluids* 173 (2018) 307–312, ISSN 0045-7930, .
- H. Dong, L. Fu, F. Zhang, Y. Liu, J. Liu, Detonation simulations with a fifth-order TENO scheme, *Communications in Computational Physics* 25 (2019) 1357–1393, .
- X. D. Liu, S. Osher, T. Chan, Weighted Essentially Non-oscillatory Schemes, *Journal of Computational Physics* 115 (1) (1994) 200–212, ISSN 0021-9991.
- G.-S. Jiang, C.-W. Shu, Efficient Implementation of Weighted ENO Schemes, *Journal of Computational Physics* 126 (1) (1996) 202–228, ISSN 0021-9991.
- R. Borges, M. Carmona, B. Costa, W. S. Don, An improved weighted essentially non-oscillatory scheme for hyperbolic conservation laws, *Journal of Computational Physics* 227 (6) (2008) 3191–3211, ISSN 0021-9991, .
- D. Sun, F. Qu, C. Yan, An efficient adaptive high-order scheme based on the WENO process, *Computers & Fluids* 140 (2016) 81 – 96, ISSN 0045-7930, .
- X. Deng, H. Zhang, Developing High-Order Weighted Compact Nonlinear Schemes, *Journal of Computational Physics* 165 (1) (2000) 22 – 44, ISSN 0021-9991, .
- X. Deng, H. Maekawa, Compact High-Order Accurate Nonlinear Schemes, *Journal of Computational Physics* 130 (1) (1997) 77 – 91, ISSN 0021-9991, .
- Z. Yan, H. Liu, M. Mao, H. Zhu, X. Deng, New nonlinear weights for improving accuracy and resolution of weighted compact nonlinear scheme, *Computers & Fluids* 127 (2016) 226 – 240, ISSN 0045-7930, .
- S. Zheng, X. Deng, D. Wang, C. Xie, A parameter-free ϵ -adaptive algorithm for improving weighted compact nonlinear schemes, *Int J Numer Meth Fluids* 90 (5), ISSN 0271-2091, .
- H. Zhang, F. Zhang, C. Xu, Towards optimal high-order compact schemes for simulating compressible flows, *Applied Mathematics and Computation* 355 (2019) 221–237, .
- X. Deng, High-order accurate dissipative weighted compact nonlinear schemes, *Science in China Series A: Mathematics* 45 (3) (2002) 356, ISSN 1862-2763, .
- X. Deng, X. Liu, M. Mao, H. Zhang, Investigation on weighted compact fifth-order nonlinear scheme and applications to complex flow, in: 17th AIAA Computational Fluid Dynamics Conference, AIAA 2005-5246, Toronto, Ontario Canada, , 2005.
- T. Nonomura, K. Fujii, Effects of difference scheme type in high-order weighted compact nonlinear schemes, *Journal of Computational Physics* 228 (10) (2009) 3533 – 3539, ISSN 0021-9991, .
- S. Clain, S. Diot, R. Loubère, A high-order finite volume method for systems of conservation laws–Multi-dimensional Optimal Order Detection (MOOD), *Journal of Computational Physics* 230 (10) (2011) 4028 – 4050, ISSN 0021-9991, .
- J. Zhu, C.-W. Shu, A new type of multi-resolution WENO schemes with increasingly higher order of accuracy, *Journal of Computational Physics* 375 (2018) 659 – 683, ISSN 0021-9991, .
- F. Zhang, C. Xu, J. Liu, A Simple Extending Strategy for TENO Scheme: scalar equation and Euler equations, in: *HiSST: International Conference on High-Speed Vehicle Science Technology*, Moscow, Russia, 2018.
- S. Gottlieb, C. Shu, E. Tadmor, Strong Stability-Preserving High-Order Time Discretization Methods, *SIAM Review* 43 (1) (2001) 89–112, .
- S. Pirozzoli, On the spectral properties of shock-capturing schemes, *Journal of Computational Physics* 219 (2) (2006) 489 – 497, ISSN 0021-9991, .
- C.-W. Shu, S. Osher, Efficient Implementation of Essentially Non-oscillatory Shock-capturing Schemes,II, *J. Comput. Phys.* 83 (1) (1989) 32–78, ISSN 0021-9991, .
- A. Harten, B. Engquist, S. Osher, S. R. Chakravarthy, Uniformly high order accurate essentially non-oscillatory schemes, III, *Journal of Computational Physics* 71 (2) (1987) 231–303, ISSN 0021-9991.
- F. Zhang, J. Liu, B. Chen, W. Zhong, Evaluation of rotated upwind schemes for contact discontinuity and strong shock, *Computers & Fluids* 134-135 (2016) 11–22, ISSN 0045-7930.
- F. Zhang, J. Liu, B. Chen, W. Zhong, A robust low-dissipation AUSM-family scheme for numerical shock stability on unstructured grids, *Int. J. Numer. Meth. Fluids* 84 (2017) 135–151, ISSN 1097-0363, .
- F. Qu, D. Sun, C. Yan, A new flux splitting scheme for the Euler equations II: E-AUSMPWAS for

- all speeds, *Communications in Nonlinear Science and Numerical Simulation* 57 (2018) 58–79, ISSN 1007-5704.
- D. Drikakis, S. Tsangaris, On the solution of the compressible Navier-Stokes equations using improved flux vector splitting methods, *Applied Mathematical Modelling* 17 (6) (1993) 282–297, ISSN 0307-904X.
- D. Wang, X. Deng, G. Wang, Y. Dong, Developing a hybrid flux function suitable for hypersonic flow simulation with high-order methods, *Int. J. Numer. Meth. Fluids* 81 (5) (2016) 309–327, ISSN 1097-0363.
- V. V. Rusanov, Calculation of Interaction of Non-Stationary Shock Waves with Obstacles, *Zh. Vychisl. Mat. Mat. Fiz.* 1 (2) (1961) 267–279.
- B. van Leer, Flux-Vector Splitting for the Euler Equations, in: E. Krause (Ed.), *Eighth International Conference on Numerical Methods in Fluid Dynamics*, vol. 170 of *Lecture Notes in Physics*, Springer Berlin Heidelberg, Aachen, Germany, ISSN 978-3-540-11948-7, 507–512, 1982.
- A. Harten, P. D. Lax, B. van Leer, On Upstream Differencing and Godunov-Type Schemes for Hyperbolic Conservation Laws, *SIAM Review* 25 (1) (1983) 35–61.
- G. A. Sod, A survey of several finite difference methods for systems of nonlinear hyperbolic conservation laws, *Journal of Computational Physics* 27 (1) (1978) 1–31, ISSN 0021-9991.
- P. D. Lax, Weak solutions of nonlinear hyperbolic equations and their numerical computation, *Communications on Pure and Applied Mathematics* 7 (1) (1954) 159–193, .
- D. S. Balsara, C.-W. Shu, Monotonicity Preserving Weighted Essentially Non-oscillatory Schemes with Increasingly High Order of Accuracy, *Journal of Computational Physics* 160 (2) (2000) 405 – 452, ISSN 0021-9991, .
- P. Lax, X. Liu, Solution of Two-Dimensional Riemann Problems of Gas Dynamics by Positive Schemes, *SIAM Journal on Scientific Computing* 19 (2) (1998) 319–340, .
- J. Shi, Y.-T. Zhang, C.-W. Shu, Resolution of high order WENO schemes for complicated flow structures, *Journal of Computational Physics* 186 (2) (2003) 690 – 696, ISSN 0021-9991, .
- G. Zhao, M. Sun, S. Xie, H. Wang, Numerical dissipation control in an adaptive WCNS with a new smoothness indicator, *Applied Mathematics and Computation* 330 (2018) 239 – 253, .
- N. Fleischmann, S. Adami, N. A. Adams, Numerical symmetry-preserving techniques for low-dissipation shock-capturing schemes, *Computers & Fluids* 189 (2019) 94 – 107, ISSN 0045-7930, .
- O. San, K. Kara, Evaluation of Riemann flux solvers for WENO reconstruction schemes: Kelvin-Helmholtz instability, *Computers & Fluids* 117 (2015) 24–41, ISSN 0045-7930, .